Mechanical Systems and Signal Processing 181 (2022) 109487

Contents lists available at ScienceDirect

Mechanical Systems and Signal Processing

journal homepage: www.elsevier.com/locate/ymssp

Bloch wave propagation in finitely stretched soft lattice

Shiheng Zhao [a,1], Tao Feng [a,1], Han Zhang [b], Yang Gao [a], Zheng Chang [a,*]

[a] College of Science, China Agricultural University, Beijing 100083, People's Republic of China
[b] Key Laboratory of Noise and Vibration, Institute of Acoustics, Chinese Academy of Sciences, Beijing 100190, People's Republic of China

ARTICLE INFO

Communicated by Sergio De Rosa

Keywords:
Elastic wave
Bandgap
Soft lattice
Bloch wave
Finite deformation

ABSTRACT

In this study, the in-plane Bloch wave propagation in a finitely stretched square lattice is investigated numerically and theoretically. Precisely, the elastic band diagram is calculated for an infinite periodic structure with a cruciform hyperelastic unit cell under uniaxial or biaxial tension. Meanwhile, an elastodynamic tight-binding model is proposed to investigate the formation and evolution of the band structure. In said lattice, the finite stretch was found to not only tune the symmetry of the band structure but also purify the elastic waves into easy modes. The uniaxial stretch exhibits the opposite impacts on the evolution of two easy modes, while the effect of the biaxial stretch is equated with the superposition of the uniaxial stretches in the two tessellation directions. The mentioned effects on the band structure could be attributed to the competition between the effective shear moduli and lengths for different beam components. As a result, the finite stretch could tune the directional elastic wave bandgap of the soft lattice, and the broadest bandgap could be anticipated in an equi-biaxial stretch. This study may shed some light on the design and implementation of elastic wave control devices with weight efficiency and tunability. It also reveals that the theoretically predicted flat bands did not exist in the numerical calculations, a difference between the physical system and the corresponding simplified theoretical model.

1. Introduction

Lattice materials [1] are defined as the spatially periodic networks of structural elements (e.g., beams, bars, and shells). With a highly ordered construction at different scales, such systems outperform conventional (dis-order) ones in mechanical [2–5], thermal [6–8], and other properties [9–11]. These optimized mechanical and functional materials appear extensively in nature [12–14], and meanwhile, are artificially manufactured and increasingly used as the weight-efficient structural components in diverse applications [15–19].

Over the past two decades, lattice materials have aroused considerable attention for their unique elastodynamic properties originating from the periodic arrangement and variety of microstructures. As a class of phononic crystals or metamaterials, these materials have been commonly employed to tailor the propagation of mechanical waves. Inspired by this topic, the novel wave phenomenon of lattice materials [20–26] and the effects of both material [27–29] and geometry [30–34] have been investigated. Thus far, the dynamics of lattice materials probably be considered a mature field since the governing equations and the solution techniques are extensively studied. However, as permitted by the diversity of material and structure combination and as promoted by various

* Corresponding author.
E-mail address: changzh@cau.edu.cn (Z. Chang).
[1] These authors contributed equally to the study.

https://doi.org/10.1016/j.ymssp.2022.109487
Received 4 April 2022; Received in revised form 15 June 2022; Accepted 21 June 2022
Available online 27 June 2022

technical requirements, many exciting characteristics remain to be explored.

For instance, if the solid phase exhibited by the lattice material is soft and highly deformable, more complex but fruitful wave propagation behaviors can be anticipated with subject to external mechanical loading. Accordingly, the lattice turns out to be a sophisticated wave modulation and sensing system [35,36], which suggests significant applications (e.g., non-destructive testing and health monitoring for flexible and morphable structures). In such a system, the mechanical loading can tense the network, and it acts as a robust mechanism for tunability in the preparation and use of the lattice material. As demonstrated by a spider orb-web, it forms a mechanically stable construction with taut threads [37]. The web transmits vibration signals, acting as a communication channel during the prey capture and the courtship [36,38]. Notably, tensions in an orb-web are not evenly distributed, and they can be controlled by a spider [37] when the web is being weaved and used (Spider jerks the radial threads to locate the prey.).

Most of the relevant works on the dynamics of soft phononic crystals and metamaterials concentrate on materials with high relative density [39–41] or multiple phases [42–47]. Despite reports of novel or anomalous behaviors, the underlying mechanisms remain elusive as a result of the complex material compositions and structural configurations. Even in single-phase lattices with simple geometry, such as spider webs, the wave propagation behavior under finite deformation is still poorly understood, let alone offering clear guidelines for designing wave control systems that are lightweight, flexible, and easy to fabricate. Several issues must be addressed in this topic, including: How does the mechanical loading simultaneously affect the effective (or instantaneous) material properties and geometry configuration of the soft lattice, as well as how does this further influence wave propagation? What are the critical material and geometric parameters that govern wave propagation?

To clarify the mentioned problems, this study investigates numerically and theoretically the in-plane Bloch wave propagation in a finitely stretched square lattice and determines the effects of geometric and material properties induced by the finite deformation. Specifically, in accordance with the Small-on-Large theory, numerical simulations are performed to examine the formation and evolution of the band structure. An elastodynamic tight-binding model is also proposed to provide valuable estimates and elucidate the underlying mechanisms.

The rest of this study is organized as follows. In Section 2, the model description and several theoretical backgrounds are presented (e.g., the Small-on-Large and Bloch theories). In Section 3, the numerical and theoretical methods of examining the band structure of the soft lattice are illustrated. In Section 4, the band structure, the effect of pre-deformation, together with the evolution of bandgaps are illustrated. Lastly, the brief concluding remarks are drawn in Section 5.

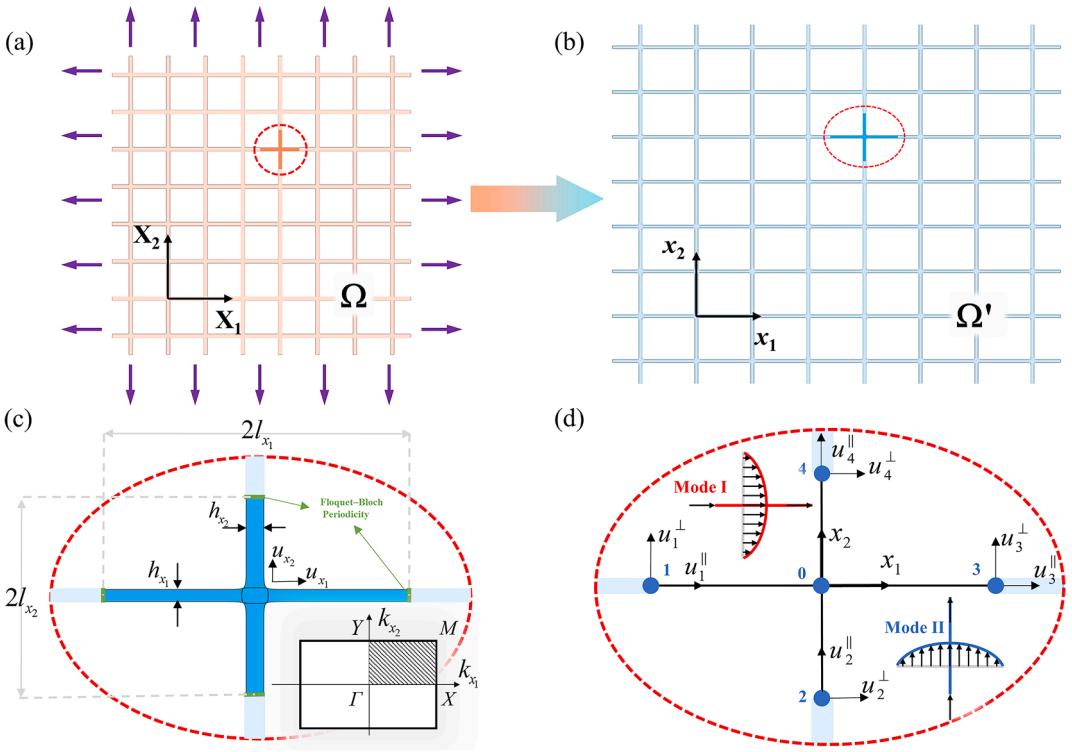

Fig. 1. Schematic diagrams of the 2D soft lattice material and its unit cell. (a) and (b) represent the initial (Ω) and current (Ω′) configurations before and after the finite deformation, respectively. (c) and (d) represent the unit cells of the current configuration adopted for the numerical and theoretical analyses, respectively. The first Irreducible Brillouin Zone (IBZ) of the unit cell applied in the Bloch wave analysis is presented in the inset of (c). The two easy wave modes are illustrated in the insets of (d).

2. Model description and theoretical background

2.1. Model description

An infinite 2D square lattice is considered, with its initial configuration Ω presented in Fig. 1(a). The unit cell is a cruciform structure rigidly connected by four flexural beams, with the related tessellation directions (lattice basis vectors) parallel to the beams' axes. The material of the respective beam is homogeneous, isotropic, and soft, so it exhibits a hyperelastic constitution. In the plane-strain assumption, the finite deformation and the incremental wave motion are constrained in the X_1X_2 plane. The lattice's macroscopic deformation is considered under the uniaxial or biaxial tensile strains in the tessellation directions for simplicity. Accordingly, the orthogonal beams hardly affected each other during the deformation, and any possible instability induced by the compression is avoided.

With the finite deformation, the soft lattice expanded to the current configuration Ω' (Fig. 1(b)), and the corresponding unit cell emerged a cruciform with diverse arm lengths (Fig. 1(c)). Except for the joint of the beams, most areas in the unit cell exhibited a state of uniaxial tension. In this fashion, the finite deformation could be expressed by the principal stretches (λ_1 and λ_2). Furthermore, the geometry of the current configuration could be characterized by the lengths (l_{x_1} and l_{x_2}) and widths (h_{x_1} and h_{x_2}) of the beams.

2.2. Theoretical background

To analyze the propagation of the Bloch wave in the soft lattice, some preliminary (e.g., the descriptions of finite deformation, incremental wave motion, and the Bloch boundary condition) are presented in the following, which are essential for both numerical and theoretical analyses.

2.2.1. Finite deformation

For a hyperelastic solid with the constitutive behavior characterized by the strain energy function W, the finite deformation makes the material particle at X_j in the reference (undeformed) configuration (Ω) move to the current position x_i in the current (deformed) configuration (Ω'). In the absence of the body force, the deformation process satisfies the equilibrium equation, i.e.,

$$\mathscr{S}_{ij,i} = 0, \tag{1}$$

where $\mathscr{S}_{ij} = \partial W/\partial F_{ji}$ denotes the nominal (or the transpose of the first *Piola-Kirchhoff*) stress tensor; $F_{ji} = \partial x_j/\partial X_i$ is the deformation gradient (unless otherwise specified, the repeated lower index complied with the Einstein summation convention). From the relationship between stress and deformation gradient, the instantaneous elastic tensor (or tangent modulus) of the material is written as

$$C_{ijkl} = \frac{\partial \mathscr{S}_{ij}}{\partial F_{lk}} = \frac{\partial^2 W}{\partial F_{ji}\partial F_{lk}}. \tag{2}$$

Thus, Eq. (1) can be expressed as

$$\left(C_{ijkl}x_{l,k}\right)_{,i} = 0. \tag{3}$$

Since C_{ijkl} is non-linearly determined by F_{ij}, Eq. (3) expresses a set of non-linear partial differential equations of the second order for x_i. Specific to a particular x_i (or equivalently F_{ij}), the uniquely determined C_{ijkl} is termed as the instantaneous elastic tensor expressed in the initial configuration. In this scenario, C_{ijkl} and F_{ij} are utilized to analyze the incremental wave motion.

2.2.2. Incremental wave motion

To examine the incremental (linear) wave motion u_i superimposed onto the finite deformation, the stress generated by the waves is neglected, the finite prestress is equated with the instantaneous material parameters (Eq. (2) and (5)), and the waves were considered to propagate in a stress-free effective medium. Thus, the governing equation of wave motion in the current configuration is expressed as [48]

$$\left(\widetilde{C}_{ijkl}u_{l,k}\right)_{,i} + \widetilde{\rho}\boldsymbol{\omega}^2 u_j = 0, \tag{4}$$

where $\boldsymbol{\omega}$ denotes the angular frequency. $\widetilde{C}_{ijkl}$ and $\widetilde{\rho}$ are determined by pushing forward on C_{ijkl} and ρ (expressed in the current configuration), respectively, [48]

$$\widetilde{C}_{IjKl} = J^{-1}F_{Ii}F_{Kk}C_{ijkl}, \widetilde{\rho} = \mathrm{J}^{-1}\rho, \tag{5}$$

where $J = \det\left(F_{ij}\right)$ denotes the volumetric ratio. As opposed to Eq. (3), Eq. (4) expresses a set of linear partial differential equations of the second order foru_i.

2.2.3. Bloch boundary condition

To determine the spatial periodicity of the current configuration, a set of lattice vectors $\vec{a}_s$ ($s = x_1, x_2$) are defined, so an arbitrary

unit cell could be indexed with the vector $r_s = n_{\underline{s}}|a_{\underline{s}}|$, with n_s as an integer (the underlining represents that the Einstein summation convention is not invoked). Accordingly, the position of any point x_s^0 in a unit cell is expressed as $x_s = x_s^0 + r_s$. By complying with the Bloch theorem, the Bloch periodicity for arbitrary space function ψ is defined as:

$$\psi(x_s^0 + r_s) = \psi(x_s^0)e^{ik_s r_s}, \tag{6}$$

where i denotes $\sqrt{-1}$; k_s is the wave vector in the reciprocal lattice (Fig. 1(c)).

Eqs. (4) and (6) usually form a definite solution problem of wave propagation in a periodic soft lattice, which underpinned the following numerical and theoretical analyses.

3. Methods for Bloch wave analysis

In the present section, the numerical method is presented to determine the band structure of the soft lattice. Moreover, a theoretical model is proposed to analyze the effect, together with the underlying mechanism, of the finite deformation on the Bloch wave behavior.

3.1. Numerical (Finite Element) analysis

The numerical simulations are conducted with the finite-element (FE)-method-based software COMSOL Multiphysics. With 2D plane-strain assumption applied, a two-step model [49,50] is adopted to analyze the finite deformation and the incremental wave motion, respectively. First, the finite deformation of a unit cell (Fig. 1(a)) of the soft lattice, complying with Eq. (1), was calculated through the nonlinear quasi-static analysis with the solid mechanics module. Second, with the deformed geometry (Fig. 1(c)) and the deformation gradient, which are obtained in step one, imported, the band structure of the lattice is determined with the module of weak-form PDE. Based on an eigenvalue analysis of Eq. (4), the band structure, i.e., the dispersion relation of elastic waves, is explored along the edges ($\Gamma - X - M - Y - \Gamma$) of the first Irreducible Brillouin Zone (IBZ, Fig. 1(c)). Detailed information about the numerical simulations can be referred in the Supplementary Material.

3.2. Theoretical model: An elastodynamic tight-binding model

Despite the numerical simulation, a theoretical model was also built to characterize the Bloch wave propagation and, more importantly, to qualitatively indicate the effect of finite deformation on the band structure. Thus, the unit cell was simplified as a nodal connection of four beams under the ideal uniaxially stretch. As illustrated in Fig. 1(d), the internal node was numbered as 0, and the peripheral nodes were numbered as 1–4, respectively. The indexes of the four beams were identical to the corresponding peripheral nodes. Thus, $\{u_i\|(s),\ u_i^{\perp}(s)\}, i = 1,2,3,4$ is adopted to represent the axial and transverse displacements (relative to the beam direction) in the i - th beam, where s denotes the local axial coordinate ($s = x_1$ (or x_2) for $i = 1,\ 3$ (or 2, 4)) with the origin at the central node (Fig. 1(d)).

3.2.1. Equations of motion in a single beam

For a single *Rayleigh* beam under the axial stretch, there exist two wave modes, i.e., the longitudinal (Primary, or P- for short) and transverse (Secondary, or S-) modes, which are respectively governed by the one-dimensional time-harmonic wave equations [51]

$$\widetilde{E}u_i^{\|\prime\prime}(s) + \widetilde{\rho}\omega^2 u_i\|(s) = 0, \tag{7}$$

$$B\widetilde{E}u_i^{\perp\prime\prime\prime}(s) + \left(B\widetilde{\rho}\omega^2 - \widetilde{G}\right)u_i^{\perp\prime}(s) - \widetilde{\rho}\omega^2 u_i^{\perp}(s) = 0, \tag{8}$$

where the prime represents the differentiation with respect to$s$. $B = I/A$ expresses the moment of inertia divided by the cross-sectional area. $\widetilde{E}$ and $\widetilde{G}$ are the effective Young's and shear moduli with expressions [51]

$$\widetilde{E} = \widetilde{C}_{1111} - \frac{\widetilde{C}_{1122}\widetilde{C}_{2211}}{\widetilde{C}_{2222}},\ \widetilde{G} = \widetilde{C}_{1212} - \frac{\widetilde{C}_{1221}\widetilde{C}_{2112}}{\widetilde{C}_{2121}} \tag{9}$$

in 2D problems, which measure the stiffness of a *finitely stretched* beam to resist incremental wave motion in P- and S-modes, respectively. For a specific deformation state, their value can be obtained by Eq. (5). It is also worthy of note that $\widetilde{G}$ is equivalent to the axial Cauchy stress in the *Rayleigh* beam [51]. The theoretical model ignores the irregular geometry and inhomogeneous deformation in the unit cell that distribute near the junction. By means of compensation (or numerical correction) for this simplification, we calculate $\widetilde{E}$ and $\widetilde{G}$ by using the deformation gradient of a beam component obtained from the numerical simulation instead of making a rough estimate of them with the elongation of a single beam. The comparison between these two treatments can be referred in the Supplementary Material.

3.2.2. Boundary conditions

Twenty-four boundary conditions are required to establish a proper combination of equations of motion for each beam, which includes the following:

a). Nine kinematic conditions at the internal node, representing the compatibility of displacement, i.e.,

$$u_1^p(0) = u_2^q(0) = u_3^p(0) = u_4^q(0),\ (p,q = \perp, \|,\ p \neq q), \tag{10}$$

and rotation (with rigid joint assumption), i.e.,

$$u_1^{\perp'}(0) = u_2^{\perp'}(0) = u_3^{\perp'}(0) = u_4^{\perp'}(0); \tag{11}$$

b). Three equilibrium conditions at the internal node, i.e.,

$$N_i(0) - N_{i+2}(0) + V_j(0) - V_{j+2}(0) = 0,\ (i,j = 1,2,\ i \neq j) \tag{12}$$

$$M_1(0) - M_3(0) + M_2(0) - M_4(0) = 0, \tag{13}$$

where

$$V_i(s) = -\widetilde{E}_s A_s B_s u_i^{\perp'''}(s) + \left(\widetilde{G}_s - \widetilde{\rho}_s B_s \boldsymbol{\omega}^2\right) A_s u_i^{\perp'}(s), N_i(s) = \widetilde{E}_s A_s u_i^{\|''}(s), M_i(s) = \widetilde{E}_s I_s u_i^{\perp''}(s), \tag{14}$$

denote the shear force, the axial force, and the bending moment in the i - th beam, respectively;

c). Twelve Bloch boundary conditions at the peripheral nodes, representing the periodicity of the displacement, rotation, bending moment, and shear force. In the local coordinate system, the Bloch conditions (Eq. (6)) are expressed as:

$$\boldsymbol{\Psi}_{i+2}\left(x_s^0 + r_s\right) = \boldsymbol{\Psi}_i\left(x_s^0\right) e^{ik_s r_s}. \tag{15}$$

To be specific, we take $\boldsymbol{\Psi}_i = u_i^{\perp}, u_i^{\perp'}, u_i\|, u_i^{\|'}, M_i, V_i$, $x_s^0 = -l_s$ and $r_s = 2l_s$ in Eq. (15). ($s = x_1$ (or x_2) for $i = 1,\ 3$ (or 2, 4)).

3.2.3. Assembly of equations and analytical dispersion relation

With eight equations of motion (Eqs. (7) and (8)) and twenty-four boundary conditions, an eigenvalue problem is formed with a 24×24 characteristic matrix [19]. In this study, more accurate results could be achieved by performing the numerical treatment. The theoretical model is mainly used to reveal the underlying mechanism. However, such a huge algebraic system could be too complicated to yield an analytical solution concise enough for qualitative analyses. As a trade-off, instead of solving the characteristic determinant directly, the algebraic system is first degenerated into two smaller (12×12) systems by confining (or "binding") the possible deformation of the soft lattice into two "easy" modes. Consistent with the tight-binding model in solid physics, this degenerate model is termed as an elastodynamic "tight-binding" model. Given the mode shapes illustrated in the insets of Fig. 1(d), the two beams with identical orientation in the unit cell vibrated in a P- or S-mode, whereas the other two beams presented the counterpart mode. These mentioned modes led to the identical displacement directions of the respective material point in the unit cell and are, therefore, in a homogenization perspective, the longitudinal (P-) and transverse (S-) modes of the lattice. We refer to them as "easy" (easiest to be excited) modes to distinguish them from the propagation modes of the beam components.

The elastodynamic tight-binding model requires the rigid joint constraint at the internal node to be relaxed to construct the degenerated problem. Accordingly, the compatibility condition of rotation (Eq. (11)) is replaced with:

$$u_1^{\perp'}(0) = u_3^{\perp'}(0), \tag{16}$$

$$u_2^{\perp'}(0) = u_4^{\perp'}(0). \tag{17}$$

In correspondence, the equilibrium of bending moment (Eq. (13)) should be replaced with:

$$M_1(0) = M_3(0), \tag{18}$$

$$M_2(0) = M_4(0). \tag{19}$$

Thus, under Mode I (Fig. 1(d)), the corresponding equations of motion are Eq. (7) for $i = 1,\ 3$, and Eq. (8) for $i = 2,\ 4$. Moreover, the selected boundary conditions are Eq. (10) for$p = \|,\ q = \perp$, Eq. (12) for $i = 1, j = 2$, Eq. (15) for $s = x_1,\ i = 1,\ 3$ when $\boldsymbol{\Psi}_i = u_i\|$ and $u_i^{\|'}$, and for $s = x_2,\ i = 2,\ 4$ when $\boldsymbol{\Psi}_i = u_i^{\perp},\ u_i^{\perp'},\ M_i$ and V_i, Eqs. (17) and (19). The rest equations constituted the boundary value problem under Mode II.

3.2.4. Analytical dispersion relations

By solving the two eigenvalue problems under the easy modes, the dispersion equations, describing the propagation of Bloch waves with a frequency $\boldsymbol{\omega}$ and a wave vector k_s in the soft lattice, could be yielded. Under Modes I ($s = x_1$) and II ($s = x_2$), it yields:

$$P_s(\boldsymbol{\omega})Q_t(k_t,\boldsymbol{\omega}) + R_s(k_s,\boldsymbol{\omega})T_t(k_t,\boldsymbol{\omega}) = 0 \tag{20}$$

with $s,\ \mathrm{t} = x_1,\ x_2$ and $s \neq \mathrm{t}$, in which

$$\begin{aligned} P_s(\boldsymbol{\omega}) &= \sin\left(\frac{2l_s\sqrt{\widetilde{\rho}_s}}{\sqrt{\widetilde{E}_s}}\,\boldsymbol{\omega}\right), Q_t(k_t,\boldsymbol{\omega}) = \gamma_t\alpha_t\beta_t h_t\left(\cos(2k_t l_t) - \cosh\left(\sqrt{2}\,l_t\alpha_t\right)\right)\left(\cos(2k_t l_t) - \cosh\left(\sqrt{2}\,l_t\beta_t\right)\right), R_s(k_s,\boldsymbol{\omega}) \\ &= h_s\sqrt{2\widetilde{E}_s\widetilde{\rho}_s}\boldsymbol{\omega}\left(\cos(2k_s l_s) - \cos\left(\frac{2l_s\sqrt{\widetilde{\rho}_s}}{\sqrt{\widetilde{E}_s}}\,\boldsymbol{\omega}\right)\right), T_t(k_t,\boldsymbol{\omega}) \\ &= \sinh\left(\sqrt{2}\,l_t\beta_t\right)\alpha_t\left(\cos(2k_t l_t) - \cosh\left(\sqrt{2}\,l_t\alpha_t\right)\right) \qquad - \sinh\left(\sqrt{2}\,l_t\alpha_t\right)\beta_t\left(\cos(2k_t l_t)\right. \\ &\quad \left. - \cosh\left(\sqrt{2}\,l_t\beta_t\right)\right), \end{aligned} \tag{21}$$

and $\alpha_t,\ \beta_t,\ \gamma_t$ are defined as:

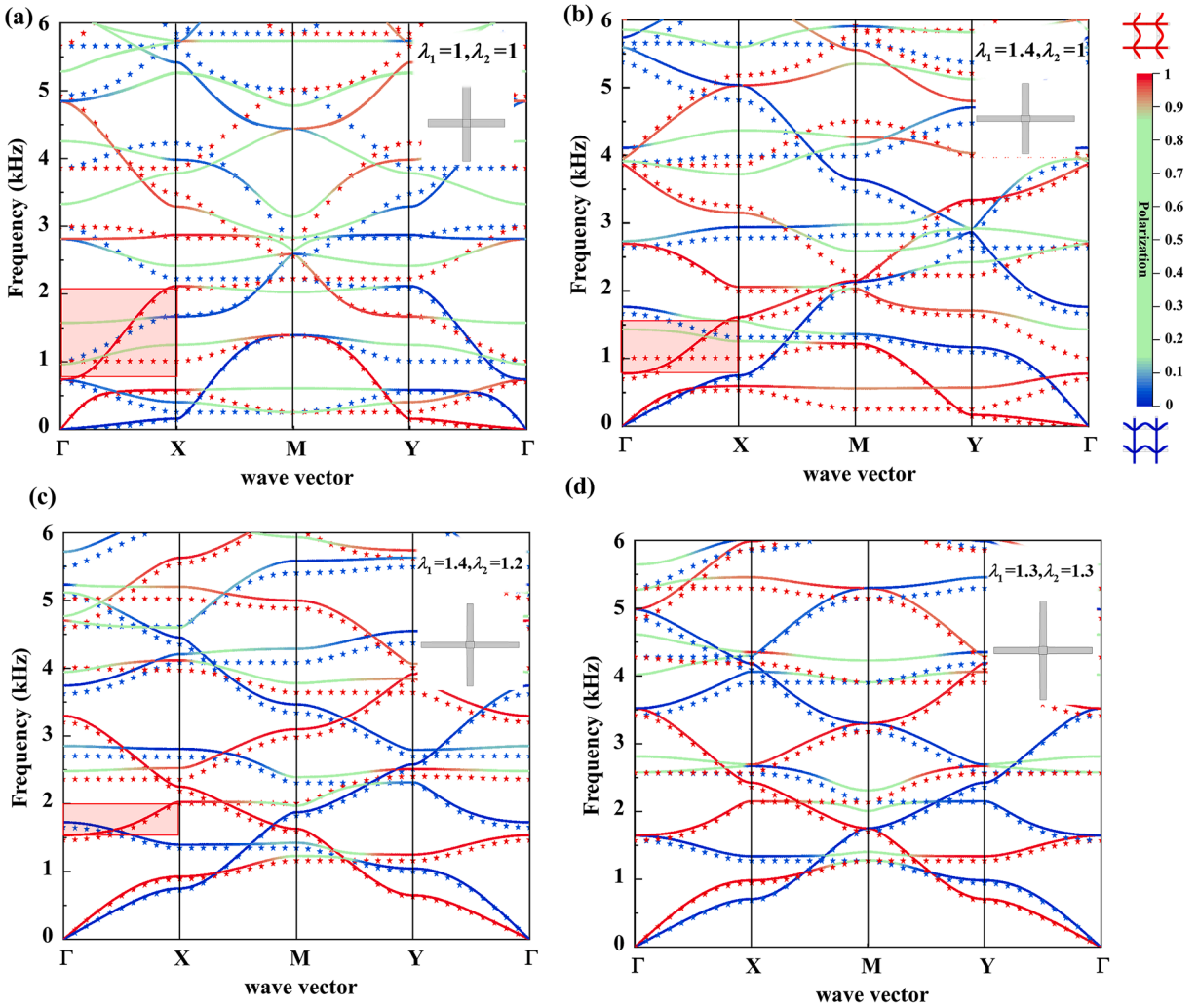

Fig. 2. Phononic band structures for the soft lattice with the typical finite deformation conditions: (a) deformation free ($\lambda_1 = \lambda_2 = 1$), (b) uniaxial stretch ($\lambda_1 = 1.4,\ \lambda_2 = 1$), (c) biaxial stretch ($\lambda_1 = 1.4,\ \lambda_2 = 1.2$), and (d) equi-biaxial stretch ($\lambda_1 = \lambda_2 = 1.3$). The solid and scattered lines denote the numerical (FE) and theoretical results, respectively. The colors in the lines indicate the magnitude of the polarization, from 0 (Mode II) to 1 (Mode I). A typical branch in $\Gamma - X$ interval was marked with red shading in (a), (b) and (d), respectively, to show its evolution with the deformation. (For interpretation of the references to colour in this figure legend, the reader is referred to the web version of this article.)

$$\alpha_t = \sqrt{\frac{\widetilde{G}_t - B_t\widetilde{\rho}_t\omega^2 + \gamma_t}{B_t\widetilde{E}_t}}, \beta_t = \sqrt{\frac{\widetilde{G}_t - B_t\widetilde{\rho}_t\omega^2 - \gamma_t}{B_t\widetilde{E}_t}}, \gamma_t = \sqrt{4B_t\widetilde{E}_t\widetilde{\rho}_t\omega^2 + \left(\widetilde{G}_t - B_t\widetilde{\rho}_t\omega^2\right)^2}. \tag{22}$$

Specific to non-zero R_s andQ_t, Eq. (20) is rewritten as:

$$\frac{P_s(\boldsymbol{\omega})}{R_s(k_s,\boldsymbol{\omega})} + \frac{T_t(k_t,\boldsymbol{\omega})}{Q_t(k_t,\boldsymbol{\omega})} = 0, \tag{23}$$

revealing the decoupling of the horizontal and vertical beam components for any frequency $\boldsymbol{\omega}$, i.e., the stretch in the s-direction only changes the terms or parameters with subscript s, with the remaining unaffected. Whereas for $Q_t = 0$ or $R_s = 0$, the flat bands, i.e., resonance modes independent of the wave vector, were present in different edges of IBZ.

As reported in the existing study on a single soft beam [51], a sufficiently large stretch might lead to $B \to 0$ and $\widetilde{G} \to \widetilde{E}$. When $B \to 0$, the rotary motion of beam elements is negligible, and Eq. (8) degenerated to the identical form as Eq. (7). Thus, the dispersion relation is simplified to a certain extent. For instance, when the beams in both directions are under large stretches, i.e., $B_t \to 0$, the band structure (Eq. (20)) is simplified as:

$$\sqrt{\widetilde{G}_t}\widetilde{\rho}_t \sin\left(\frac{2l_s\sqrt{\widetilde{\rho}_s}}{\sqrt{\widetilde{E}_s}}\boldsymbol{\omega}\right)\left(\cos(2k_tl_t) - \cos\left(\frac{2l_t\sqrt{\widetilde{\rho}_t}}{\sqrt{\widetilde{G}_t}}\boldsymbol{\omega}\right)\right) + \sqrt{\widetilde{E}_s}\widetilde{\rho}_s \sin\left(\frac{2l_t\sqrt{\widetilde{\rho}_t}}{\sqrt{\widetilde{G}_t}}\boldsymbol{\omega}\right)\left(\cos(2k_sl_s) - \cos\left(\frac{2l_s\sqrt{\widetilde{\rho}_s}}{\sqrt{\widetilde{E}_s}}\boldsymbol{\omega}\right)\right) = 0. \tag{24}$$

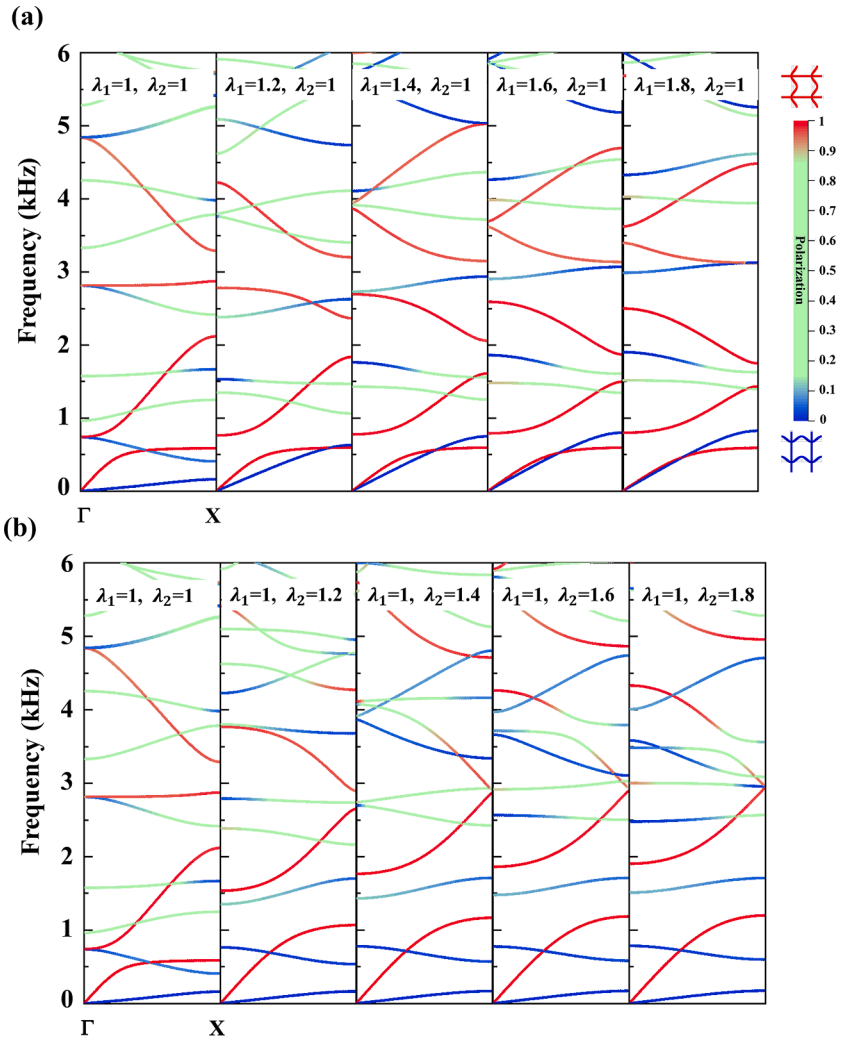

Fig. 3. Effect of uniaxial stretch on the band diagram in the $\Gamma - X$ direction. (a) and (b) represent the numerical results for the deformation applied in the x_1- and x_2-directions. The colors in the lines indicate the magnitudes of the polarization.

Accordingly, $\widetilde{G} \to \widetilde{E}$ further simplified the dispersion relation. When $\widetilde{G}_s = \widetilde{E}_s$, Eq. (24) presents an identical form for $s = x_1$ and x_2, which indicates an overlap of the band curves under Modes I and II.

4. Band structure of the soft lattice

In the subsequent calculations, the geometry parameters of the unit cell at initial configuration are taken as $2l_{x_1} = 2l_{x_2} = 10h_{x_1} = 10h_{x_2} = 0.01$ m. A hyperelastic material with compressible neo-Hookean strain energy function, i.e., [49]

$$W = \frac{\mathscr{L}}{2}(J-1)^2 - \mu \ln J + \frac{\mu}{2}\left(\mathrm{tr}(F_{si}F_{sj}) - 2\right), \tag{25}$$

is considered, where $\mathscr{L}$ and μ denote the first and second Lamé constants, respectively. The initial material parameters are assumed with the first and second Lamé constants $\mathscr{L} = 7$ MPa, $\mu = 1$ MPa, respectively, as well as the initial mass density $\rho = 1110$ kg/m^3. The mentioned parameters denote a melt-processible rubber [52]. The material damping is neglected for simplicity.

4.1. Band structure for typical finite deformation

The band structure of the soft lattice under the typical finite deformation conditions is illustrated in Fig. 2. To classify the wave modes of each branch, the amount of polarization is defined as [53]:

$$p^2 = \frac{\int |u_{x_1}|^2 \mathrm{d}r}{\int \left(|u_{x_1}|^2 + |u_{x_2}|^2\right)\mathrm{d}r}, \tag{26}$$

where the integral takes over the current configuration of the unit cell (the cyan-blue area in Fig. 1(c)), u_{x_1} and u_{x_2} represent the displacement components (Fig. 1(c)). For the in-plane wave motion, $p^2 = 0$ or $p^2 = 1$ represent two easy modes, whereas the value between 0 and 1 represents the coupled mode (In Figs. 2, 3, and 5, we display $p^2 \in [0.15,\ 0.85]$ in green without any distinction, which is easy to observe). Then, the easy modes predicted with the theoretical model are also provided.

The band structure of the deformation-free lattice ($\lambda_1 = \lambda_2 = 1$) is demonstrated in Fig. 2(a). As indicated from the comparison of the numerical and theoretical results, the theoretical model reasonably captures the essential characteristics of the propagation of Bloch waves in the soft lattice, especially for easy modes. However, when the lattice wave propagated under the coupled mode, the theoretical prediction slightly deviated from the numerical simulation.

The band structures of the lattice under the uniaxial ($\lambda_1 = 1.4,\ \lambda_2 = 1$), biaxial ($\lambda_1 = 1.4,\ \lambda_2 = 1.2$), and equi-biaxial ($\lambda_1 = \lambda_2 = 1.3$) stretches are respectively illustrated in Fig. 2(b)–(d), demonstrating that the elongation in different tessellation directions diversely impacted the movement of the bands. As the comparison of Fig. 2(a)–(c), the proportion of the coupled modes (green curves) in the band structure decreased significantly by the stretches, which suggests that the finite deformation could purify the wave modes

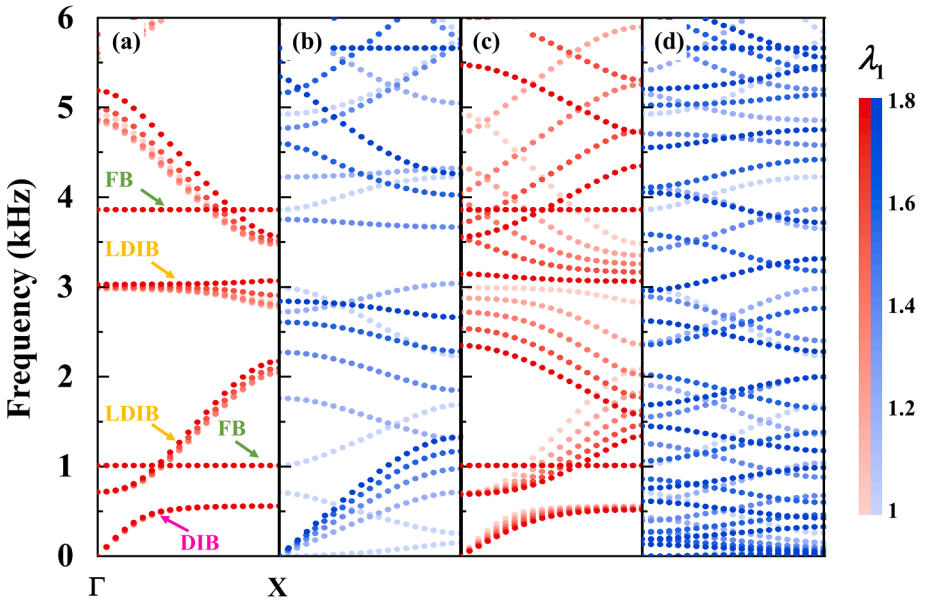

Fig. 4. The effect of material (a & b) and geometrical (c & d) factors on the band structure, in which the diagrams for P- (red) and S- (blue) modes are presented independently, and the colors represent the magnitude of the uniaxial stretch. (For interpretation of the references to colour in this figure legend, the reader is referred to the web version of this article.)

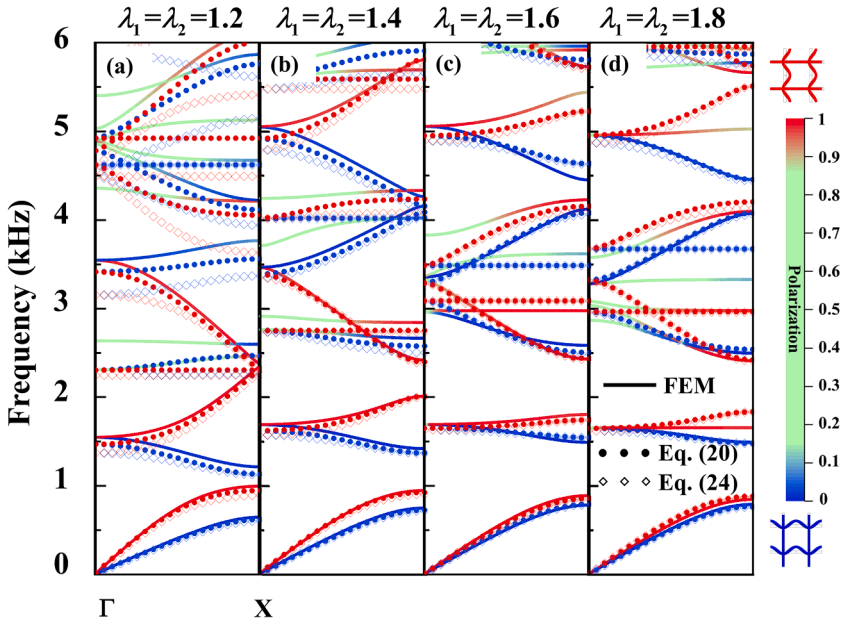

Fig. 5. The comparison of the band diagram in the Γ −*X* interval under equi-biaxial stretch, obtained from numeral simulation (solid lines), Eq. (20) (solid scatters), and Eq. (24) (hollow scatters), respectively.

(i.e., turn the coupled modes into easy ones). Note that "purify" here refers specifically to mode conversion that results from finite stretch, as opposed to "filtering," which is very common in phononic crystals. It also reveals that the theoretical model is more suitable for predicting the band structure of the pre-deformed lattice than that of the undeformed one. For the equi-biaxial stretch (Fig. 2(d)), all the branches shifted to higher frequencies than that for deformation-free lattice, and the coupled modes are localized around the high-symmetry points.

Fig. 2 present no complete bandgaps in the frequency range of interest. However, the directional bandgaps existed under both wave modes, and their locations moved with the applied finite deformation. Besides, it is noted that the flat band and the degeneracy points are predicted in the theoretical model, whereas they are not present in the numerical results. In the following subsections, all the mentioned phenomena will be discussed more specifically.

4.2. *Effect of pre-deformation on the band structure*

4.2.1. *The effect of uniaxial stretch*

To reveal the effect of finite deformation on the soft lattice's band structure, the band diagram are drawn in **Γ** −*X* interval with uniaxial stretch $\lambda = 1 \sim 1.8$ applied in x_1- and x_2-directions in Fig. 3(a) and (b), respectively. As revealed from the figure, the stretch along the x_1-direction decreased the eigenfrequencies under Mode I, whereas it increases the eigenfrequencies under Mode II. However, the x_2-counterpart exerted an opposite effect. Under the coupled mode, no significant regularity is observed.

The theoretical model qualitatively explains the evolution pattern. When $s = x_1$, Eq. (24) concludes that $\omega \propto \sqrt{\widetilde{E}_{x_1}/\widetilde{\rho}_{x_1}}/l_{x_1}$ under Mode I and $\omega \propto \sqrt{\widetilde{G}_{x_1}/\widetilde{\rho}_{x_1}}/l_{x_1}$ under Mode II. As indicated from the further analysis (Supplementary Material), both $\widetilde{G}_{x_1}$ and l_{x_1} increase after a certain tensile deformation, while $\widetilde{E}_{x_1}$ and $\widetilde{\rho}_{x_1}$ remain almost unchanged. Moreover, the variation of $\sqrt{\widetilde{G}_{x_1}}$ is more significant than that of l_{x_1}. In summary, $\widetilde{G}_{x_i}$ and l_{x_i} determine the band shift. After a stretch along the x_1 (or x_2)-direction, the eigenfrequencies under Mode I decreased by the increment of l_{x_1} (or $\sqrt{\widetilde{G}_{x_2}}/l_{x_2}$), while that under Mode II increased by the increment of $\sqrt{\widetilde{G}_{x_1}}/l_{x_1}$ (or l_{x_2}).

The effect of the finite pre-deformation on soft lattice material involved the variations in (effective) material and geometry. To consult their influence separately, under the uniaxial stretch (Fig. 3(a)), the band diagram is recalculated by using the theoretical model with the initial geometric parameters and the effective material parameters after the deformation (Fig. 4). Furthermore, the band diagram obtained using the current geometric and initial material parameters is presented as a comparison.

The diagram clearly illustrates the distinct effects of geometry and material on the two easy modes under the stretch. Moreover, the evolution of the branches could be qualitatively explained by the tight-binding model. According to Fig. 4(a) and (b), the material factor exerted the opposite effects on the two wave modes: Under Mode I, the non-flat bands slightly shifted to higher frequencies with the increment of $\sqrt{\widetilde{E}_{x_1}/\widetilde{\rho}_{x_1}}$; under Mode II, however, all the eigenfrequencies, primarily affected by $\sqrt{\widetilde{G}_{x_1}/\widetilde{\rho}_{x_1}}$, increased significantly. However, the effect of the geometric factors is nearly identical for the two modes (Fig. 4(c) and (d)): The reduction in length l_{x_1}

decreased all the eigenfrequencies, and the variation is more significant for high-frequency branches than that of the lower ones. By interpreting the numerical result (Fig. 3 (a)) with the mentioned mechanisms, it is concluded that the band structure evolution resulted from the competition between material and geometric factors.

As indicated in Fig. 4(a) and (c), several anomalous bands could be perceived in the theoretical results under Mode I, including the deformation immune bands (DIBs), the local deformation immune bands (LDIBs), the flat bands (FBs). As their names suggest, the position of the DIB almost does not vary with the uniaxial stretch in the x_1-direction, while in the LDIB, only the eigenfrequency at Γ is stationary. In contrast, the dispersionless flat bands are independent of the deformation and the wave number. As indicated from the comparison of Fig. 3(a) and Fig. 4, the theoretically predicted DIBs and LDIBs are consistent with the numerical simulations. However, the flat bands never present in the numerical results. As a replacement, two coupled modes are generated by hybridizing the flat bands under Mode I and the corresponding non-flat bands under Mode II. The occurrence of these anomalous bands is explained in the Supplementary Material.

4.2.2. *The effect of biaxial stretch*

As impacted by the uncoupling of beam components in the orthogonal directions, the effect of a biaxial stretch was equivalent to that of two sequential uniaxial stretches so that it could be qualitatively predicted. For instance, the movement of a representative branch is tracked under Mode I, which is marked with red shading in Fig. 2. A horizontal stretch to $\lambda_1 = 1.4$ make the branch move monotonically downward (Fig. 2(b)), except that its left end was almost stationary. Subsequently, a vertical stretch to $\lambda_2 = 1.2$ make the entire branch shift to higher frequencies (Fig. 2(c)).

The band diagrams of the soft lattice in $\Gamma - X$ interval for different equi-biaxial states ($\lambda_1 = 1.2 \sim 1.8$) are illustrated in Fig. 5. For comparisons, the band curves predicted by using Eq. (20) and (24) are plotted, thereby indicating that the band curves moved closer to each other with the increase in the magnitude of stretch. They almost coincide with each other when $\lambda_1 = \lambda_2$ reaches1.4. It is therefore indicated that the finite stretch weakened the rotary motion in a soft beam component. Accordingly, as a waveguide, the pre-stretched beam behaved more like a string than a *Rayleigh* beam. Furthermore, Fig. 5 demonstrates the propinquity of the two easy modes attributed to the agreement of the effective material parameters under the huge stretch. Obviously, the phenomenon could contribute to the modulation of the directional bandgap to a broad frequency range.

4.3. *The evolution of directional bandgaps under stretch*

To demonstrate the effect of pre-stretch on the bandgaps, the evolution diagrams of the bandgaps in $\Gamma - X$ interval are drawn under Modes I and II at different stretching states (Fig. 6(a) and (b)). In both figures, the frequency ranges occupied by the coupled modes are

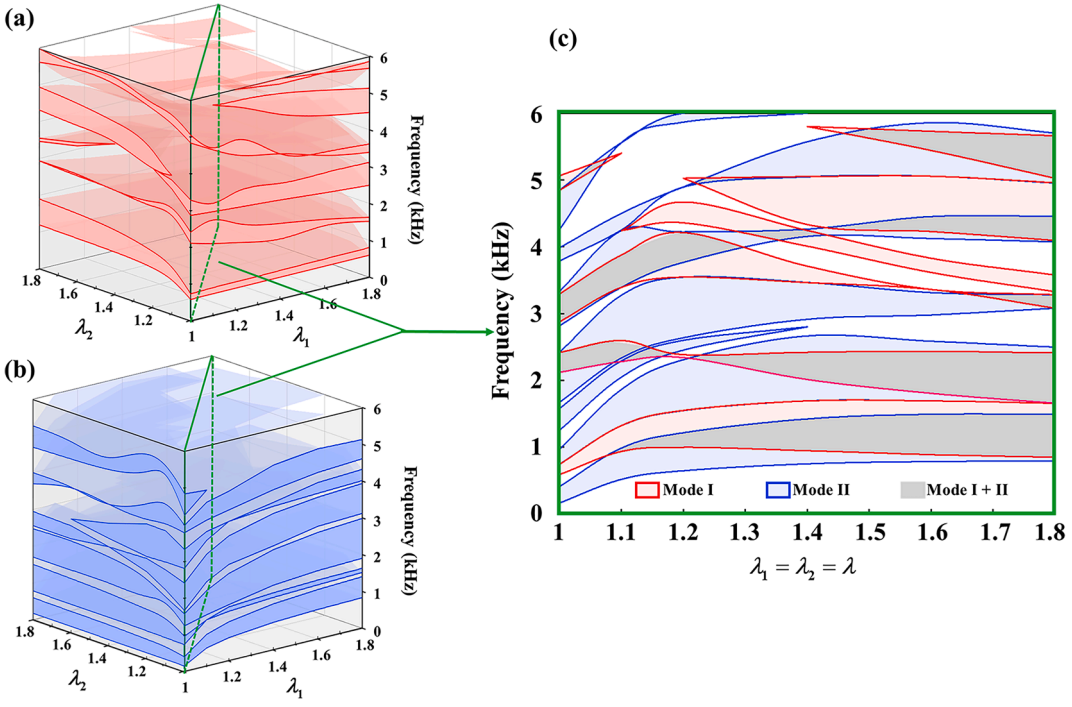

Fig. 6. Evolution of bandgaps in $\Gamma - X$ edge of IBZ with different finite deformation. (a) and (b) are the bandgap evolution under Modes I (red) and II (blue). (c) is the same as (a) and (b) but under equi-biaxial stretch. The gray areas in (c) correspond to the elastic wave bandgaps, which is the intersection of the red and blue ones. (For interpretation of the references to colour in this figure legend, the reader is referred to the web version of this article.)

passbands.

Under Mode I (Fig. 6(a)), the uniaxial stretch in the x_1-direction narrowed several (the third and fourth) of the bandgaps without affecting their center frequencies, while the x_2-counterpart simultaneously increases the bandwidths and center frequencies. As opposed to Mode I, Mode II (Fig. 6(a)) has more bandgaps in this interval. Moreover, the uniaxial stretch in either direction significantly increase the bandwidth, and the center frequencies slightly or significantly increase for the stretches in x_1- and x_2-directions, respectively. The boundaries of different bandgaps are significantly close under a huge stretch, thereby forming an ultra-wide bandgap with several narrow passbands.

Besides, the broadest in-plane elastic wave bandgap (the bandgap for both modes) appears in the case of the equi-biaxial stretch. As indicated in Fig. 6(c), the bandgaps under Mode I widened dramatically with the increase in the stretch. The two lowest bandgaps for both modes are consistent, thereby forming the widest elastic wave bandgaps at a high strain level. The mentioned phenomenon can be explained as the convergence of the dispersion curves of the two modes under a large stretch (Eq. (24) and Fig. 5(d)).

5. Conclusion and discussion

In brief, this study investigated the propagation of Bloch waves in a pre-stretched square lattice material. In this regard, the wave behavior and its influence by the finite deformation are determined by numerical simulations, while an elastodynamic tight binding model reveals the mechanism underlying the phenomena. The pre-stretched square lattice has been found to evidence the following features in terms of wave dynamics.

- In-plane elastic waves primarily propagate in two easy modes and the pre-stretch purifies the wave modes and localizes the coupled modes to the high-symmetry points.
- As the uniaxial pre-stretch increased, the two easy modes demonstrate monotonous but opposite movements. The effect of biaxial stretch falls to that of two uniaxial stretches in the tessellation directions.
- The decisive geometric and material parameters that govern the band movement represent the beam component's length and the effective shear modulus, respectively.
- The broadest directional elastic wave bandgaps appeared for the high level equi-biaxial stretch.

Though the complete bandgap does not exist in the mentioned soft lattice, it could be implemented by introducing resonance [54,55] or Bragg scattering [56] mechanisms. In addition, the comparing numerical and theoretical calculations indicated the differences between the physical and simplified theoretical models. It is therefore demonstrated that the theoretically predicted flat bands, the characteristics showing promising applications in topological acoustics [57], were not presented in the numerical calculations. However, it is not excluded that such characteristics can be determined by means, e.g., tuning the slenderness of the beam components [20]. It is worth mentioning that, in this work, the material damping is neglected for simplicity. A rough estimate (in the Supplementary Material) and two previous works [58,59] show that material loss will result in a slight band shift in a weakly coupled soft system (such as the soft lattice considered in this work) but will not cause any qualitative change in the band structure.

Hopefully, this study may present more insights into the elastodynamics of soft lattice materials and into the ways their behavior can be exploited in engineering design. Furthermore, the authors hope that this study can elucidate the design and optimization of lightweight, tunable elastic wave manipulation devices.

Declaration of Competing Interest

The authors declare that they have no known competing financial interests or personal relationships that could have appeared to influence the work reported in this paper.

Acknowledgments

This work was supported by the National Natural Science Foundation of China (Grant No.11602294) and the 2115 Talent Development Program of China Agricultural University.

Appendix A. Supplementary data

Supplementary data to this article can be found online at https://doi.org/10.1016/j.ymssp.2022.109487.

References

[1] A.S. Phani, M.I. Hussein, Dynamics of Lattice Materials, Wiley, United Kingdom, 2017.
[2] A. Casalotti, F. D'Annibale, G. Rosi, Multi-scale design of an architected composite structure with optimized graded properties, Compos. Struct. 252 (2020), 112608.

[3] T.A. Schaedler, A.J. Jacobsen, A. Torrents, A.E. Sorensen, J. Lian, J.R. Greer, L. Valdevit, W.B. Carter, Ultralight metallic microlattices, Science 334 (2011) 962–965.
[4] Q. Zhang, X. Yang, P. Li, G. Huang, S. Feng, C. Shen, B. Han, X. Zhang, F. Jin, F. Xu, T.J. Lu, Bioinspired engineering of honeycomb structure – Using nature to inspire human innovation, Prog. Mater. Sci. 74 (2015) 332–400.
[5] T. Zhang, J.M. Schwarz, M. Das, Mechanics of anisotropic spring networks, Phys. Rev. E 90 (2014), 062139.
[6] K. Wei, H. Chen, Y. Pei, D. Fang, Planar lattices with tailorable coefficient of thermal expansion and high stiffness based on dual-material triangle unit, J. Mech. Phys. Solids 86 (2016) 173–191.
[7] S. Yun, J. Kwon, D. Lee, H.H. Shin, Y. Kim, Heat transfer and stress characteristics of additive manufactured FCCZ lattice channel using thermal fluid-structure interaction model, Int. J. Heat Mass Transfer 149 (2020), 119187.
[8] K. Zhang, C. Zhao, J. Luo, Y. Ma, Z. Deng, Analysis of temperature-dependent wave propagation for programmable lattices, Int. J. Mech. Sci. 171 (2020), 105372.
[9] S.M. Montgomery, S. Wu, X. Kuang, C.D. Armstrong, C. Zemelka, Q. Ze, R. Zhang, R. Zhao, H.J. Qi, Magneto-mechanical metamaterials with widely tunable mechanical properties and acoustic bandgaps, Adv. Funct. Mater. 31 (2020) 2005319.
[10] X. Xia, A. Afshar, H. Yang, C.M. Portela, D.M. Kochmann, C.V. Di Leo, J.R. Greer, Electrochemically reconfigurable architected materials, Nature 573 (2019) 205–213.
[11] M.D. Huntington, L.J. Lauhon, T.W. Odom, Subwavelength lattice optics by evolutionary design, Nano Lett. 14 (2014) 7195–7200.
[12] M.C. Fernandes, J. Aizenberg, J.C. Weaver, K. Bertoldi, Mechanically robust lattices inspired by deep-sea glass sponges, Nat. Mater. 20 (2021) 237–241.
[13] M.C. Gibson, A.B. Patel, R. Nagpal, N. Perrimon, The emergence of geometric order in proliferating metazoan epithelia, Nature 442 (2006) 1038–1041.
[14] Y. Guo, Z. Chang, B. Li, Z.L. Zhao, H.P. Zhao, X.Q. Feng, H.J. Gao, Functional gradient effects on the energy absorption of spider orb webs, Appl. Phys. Lett. 113 (2018), 103701.
[15] T. Chen, M. Pauly, P.M. Reis, A reprogrammable mechanical metamaterial with stable memory, Nature 589 (2021) 386–390.
[16] Y. Chen, T. Li, F. Scarpa, L. Wang, Lattice metamaterials with mechanically tunable poisson's ratio for vibration control, Phys. Rev. Appl. 7 (2017), 024012.
[17] B.M. Goldsberry, S.P. Wallen, M.R. Haberman, Non-reciprocal wave propagation in mechanically-modulated continuous elastic metamaterials, J. Acoust. Soc. Am. 146 (2019) 782–788.
[18] X. Li, Y. Chen, R. Zhu, G. Huang, An active meta-layer for optimal flexural wave absorption and cloaking, Mech. Syst. Sig. Process. 149 (2021), 107324.
[19] Z. Wu, W. Liu, F. Li, C. Zhang, Band-gap property of a novel elastic metamaterial beam with X-shaped local resonators, Mech. Syst. Sig. Process. 134 (2019), 106357.
[20] G. Bordiga, L. Cabras, D. Bigoni, A. Piccolroaz, Free and forced wave propagation in a Rayleigh-beam grid: flat bands, dirac cones, and vibration localization vs isotropization, Int. J. Solids Struct. 161 (2019) 64–81.
[21] G. Bordiga, L. Cabras, A. Piccolroaz, D. Bigoni, Dynamics of prestressed elastic lattices: homogenization, instabilities, and strain localization, J. Mech. Phys. Solids 146 (2021) 104198.
[22] D. Karličić, M. Cajić, S. Paunović, S. Adhikari, Bloch waves in an array of elastically connected periodic slender structures, Mech. Syst. Sig. Process. 155 (2021), 107591.
[23] S. Sepehri, H. Jafari, M.M. Mashhadi, M.R.H. Yazdi, M.M.S. Fakhrabadi, Small-scale effects on wave propagation in planar micro-lattices, J. Sound Vibrat. 494 (2021), 115894.
[24] X. An, H. Fan, C. Zhang, Elastic wave and vibration bandgaps in planar square metamaterial-based lattice structures, J. Sound Vibrat. 475 (2020), 115292.
[25] A. Piccolroaz, A.B. Movchan, L. Cabras, Dispersion degeneracies and standing modes in flexural waves supported by Rayleigh beam structures, Int. J. Solids Struct. 109 (2017) 152–165.
[26] A.F. Russillo, G. Failla, Wave propagation in stress-driven nonlocal Rayleigh beam lattices, Int. J. Mech. Sci. 215 (2022), 106901.
[27] B.M. Goldsberry, M.R. Haberman, Negative stiffness honeycombs as tunable elastic metamaterials, J. Appl. Phys. 123 (2018), 091711.
[28] Z. Zhang, T. Li, Z. Wang, Y. Tang, Band gap characteristics of flexural wave of two-dimensional periodic frame structure composed of locally resonant composite beam, Mech. Syst. Sig. Process. 131 (2019) 364–380.
[29] L. Tang, L. Cheng, Impaired sound radiation in plates with periodic tunneled Acoustic Black Holes, Mech. Syst. Sig. Process. 135 (2020), 106410.
[30] Y.L. Huang, N. Gao, W.Q. Chen, R.H. Bao, Extension/compression-controlled complete band gaps in 2D chiral square-lattice-like structures, Acta Mech. Solida Sin. 31 (2018) 51–65.
[31] M.J. Leamy, Exact wave-based Bloch analysis procedure for investigating wave propagation in two-dimensional periodic lattices, J. Sound Vibrat. 331 (2012) 1580–1596.
[32] G. Trainiti, J.J. Rimoli, M. Ruzzene, Wave propagation in undulated structural lattices, Int. J. Solids Struct. 97–98 (2016) 431–444.
[33] A.S. Phani, J. Woodhouse, N.A. Fleck, Wave propagation in two-dimensional periodic lattices, J. Acoust. Soc. Am. 119 (2006) 1995–2005.
[34] S. Timorian, M. Ouisse, N. Bouhaddi, S. De Rosa, F. Franco, Numerical investigations and experimental measurements on the structural dynamic behaviour of quasi-periodic meta-materials, Mech. Syst. Sig. Process. 136 (2020), 106516.
[35] H.K. Zhang, X.Q. Feng, Buckling-regulated bandgaps of soft metamaterials with chiral hierarchical microstructure, Extreme Mech. Lett. 43 (2021), 101166.
[36] B. Mortimer, A. Soler, C.R. Siviour, R. Zaera, F. Vollrath, Tuning the instrument: sonic properties in the spider's web, J. R. Soc. Interface 13 (122) (2016) 20160341.
[37] E. Wirth, F.G. Barth, Forces in the spider orb web, J. Comp. Physiol., A 171 (1992) 359–371.
[38] M.A. Landolfa, F.G. Barth, Vibrations in the orb web of the spider Nephila clavipes: cues for discrimination and orientation, J. Comp. Physiol. A 179 (1996) 493–508.
[39] K. Bertoldi, M.C. Boyce, Wave propagation and instabilities in monolithic and periodically structured elastomeric materials undergoing large deformations, Phys. Rev. B 78 (2008), 184107.
[40] N. Gao, J. Li, R.-H. Bao, W.-Q. Chen, Harnessing uniaxial tension to tune Poisson's ratio and wave propagation in soft porous phononic crystals: an experimental study, Soft Matter 15 (14) (2019) 2921–2927.
[41] G.S. Sharma, A. Skvortsov, I. MacGillivray, N. Kessissoglou, Acoustic performance of periodic steel cylinders embedded in a viscoelastic medium, J. Sound Vibrat. 443 (2019) 652–665.
[42] V.F. Dal Poggetto, A.L. Serpa, Flexural wave band gaps in a ternary periodic metamaterial plate using the plane wave expansion method, J. Sound Vibrat. 495 (2021), 115909.
[43] N. Arora, Y. Xiang, S. Rudykh, Multiscale analysis of elastic waves in soft materials: from molecular chain networks to fiber composites, Int. J. Mech. Sci. 200 (2021), 106433.
[44] P. Zhang, W.J. Parnell, Soft phononic crystals with deformation-independent band gaps, Proc. Math Phys. Eng. Sci. 473 (2017) 20160865.
[45] N. Kumar, S. Pal, Unraveling interactions of resonances for tunable low frequency bandgap in multiphase metamaterials under applied deformation, Int. J. Solids Struct. 212 (2021) 169–201.
[46] D. Karličić, M. Cajić, T. Chatterjee, S. Adhikari, Wave propagation in mass embedded and pre-stressed hexagonal lattices, Compos. Struct. 256 (2021), 113087.
[47] E.G. Barnwell, W.J. Parnell, I.D. Abrahams, Antiplane elastic wave propagation in pre-stressed periodic structures; tuning, band gap switching and invariance, Wave Motion 63 (2016) 98–110.
[48] R.W. Ogden, Incremental statics and dynamics of pre-stressed elastic materials, in: M. Destrade, G. Saccomandi (Eds.), CISM Courses and LecturesWaves in Nonlinear Pre-Stressed Materials, Springer Vienna, Vienna, 2007, pp. 1–26.
[49] L.L. Chen, Z. Chang, T.Y. Qin, Elastic wave propagation in simple-sheared hyperelastic materials with different constitutive models, Int. J. Solids Struct. 126 (2017) 1–7.
[50] Z. Chang, H.Y. Guo, B. Li, X.Q. Feng, Disentangling longitudinal and shear elastic waves by neo-Hookean soft devices, Appl. Phys. Lett. 106 (2015), 161903.
[51] S.H. Zhao, Z. Chang, Elastic wave velocities in finitely pre-stretched soft fibers, Int. J. Solids Struct. 233 (2021), 111208.

[52] CES EduPack software Granta Design Limited 2019 Cambridge UK.
[53] Y. Achaoui, A. Khelif, S. Benchabane, V. Laude, Polarization state and level repulsion in two-dimensional phononic crystals and waveguides in the presence of material anisotropy, J. Phys. D: Appl. Phys. 43 (2010), 185401.
[54] C.W. Muhammad, J.T.H. Lim, Z. Li, Zhao, Lightweight architected lattice phononic crystals with broadband and multiband vibration mitigation characteristics, Extreme Mech. Lett. 41 (2020), 100994.
[55] W. Liu, J.W. Chen, X.Y. Su, Local resonance phononic band gaps in modified two-dimensional lattice materials, Acta Mech. Sin. 28 (2012) 659–669.
[56] K. Zhang, C. Zhao, P. Zhao, J. Luo, Z. Deng, Wave propagation properties of rotationally symmetric lattices with curved beams, J. Acoust. Soc. Am. 148 (2020) 1567.
[57] H. Ge, M. Yang, C. Ma, M.H. Lu, Y.F. Chen, N. Fang, P. Sheng, Breaking the barriers: advances in acoustic functional materials, Natl. Sci. Rev. 5 (2018) 159–182.
[58] R.D. Harold Berjamin Pascalis, Acoustoelastic analysis of soft viscoelastic solids with application to pre-stressed phononic crystals Int. J. Solids Struct. 241 (2021) 111529.
[59] P. Wang, F. Casadei, S. Shan, J.C. Weaver, K. Bertoldi, Harnessing buckling to design tunable locally resonant acoustic metamaterials, Phys Rev Lett 113 (2014), 014301.